OPTICS

Quantum coherence–driven self-organized criticality and nonequilibrium light localization

Kosmas L. Tsakmakidis,[1]* Pankaj K. Jha,[1]* Yuan Wang,[1] Xiang Zhang[1,2]†

Self-organized criticality emerges in dynamical complex systems driven out of equilibrium and characterizes a wide range of classical phenomena in physics, geology, and biology. We report on a quantum coherence–controlled self-organized critical transition observed in the light localization behavior of a coherence-driven nanophotonic configuration. Our system is composed of a gain-enhanced plasmonic heterostructure controlled by a coherent drive, in which photons close to the stopped-light regime interact in the presence of the active nonlinearities, eventually synchronizing their dynamics. In this system, on the basis of analytical and corroborating full-wave Maxwell-Bloch computations, we observe quantum coherence–controlled self-organized criticality in the emergence of light localization arising from the synchronization of the photons. It is associated with two first-order phase transitions: one pertaining to the synchronization of the dynamics of the photons and the second pertaining to an inversionless lasing transition by the coherent drive. The so-attained light localization, which is robust to dissipation, fluctuations, and many-body interactions, exhibits scale-invariant power laws and absence of finely tuned control parameters. We also found that, in this nonequilibrium dynamical system, the effective critical "temperature" of the system drops to zero, whereupon one enters the quantum self-organized critical regime.

INTRODUCTION

The self-organization of many nonequilibrium complex systems (1) toward an "ordered" state is a profound concept in basic science, ranging from biochemistry to physics (2–4). Examples include the group movement of flocks of birds (5), motions of human crowds (6), neutrino oscillations in the early universe (7), and the formation of shapes ("morphogenesis") in biological organisms (8, 9). An intriguing trait of this nonequilibrium, driven-dissipative systems (2, 3) is that their self-organization can lead them to a phase transition and to critical behavior—a phenomenon known as self-organized criticality (SOC) (10). Unlike equilibrium phase-transition phenomena, such as superconductivity or ferromagnetism, where an exogenous control parameter (for example, temperature or pressure) needs to be precisely tuned for the phase transition to occur, no such fine-tuning is needed in SOC systems (10–13): They can self-organize and reach their critical state even when driven far away from it. Similar to all critical phenomena (14), at exactly the phase-transition point, the SOC systems are described by scale-invariant power laws with well-defined critical exponents (15). Biological extinction events, dynamics of granular or mechanical media, and nonlinear processes in astrophysics, in magnetospheric, planetary, solar, and stellar physics, and in cosmology are examples of dynamical systems exhibiting SOC behavior (10–13, 16).

As is evident from the above examples, most SOC systems studied until now have been classical, driven by a control parameter equivalent to temperature in conventional phase transitions (14) ("thermally" driven). It is thus intriguing to identify quantum-coherently controlled systems that exhibit a phase transition in a self-organized way, wherein the critical point behaves as an attractor of the dynamics. In such a nonequilibrium, self-organized critical system, it may also be possible to enter the regime of quantum SOC (11–13, 17–20)—similar to the regime of quantum criticality in equilibrium condensed matter phase transitions (21–25). For a complex system to enter such a regime, several requirements should

be fulfilled (10–17, 21–23). These include (i) the dropping of the control parameter (effective or equivalent "temperature") to zero upon application of an external coherent field (21–23), (ii) the absence of finely tuned control parameters (10, 11), (iii) automated attraction toward a nonequilibrium steady state (15, 16), (iv) emergence of scaling and power laws with well-defined critical exponents (10–12, 15), (v) statistical independence of the events ("avalanches"; compare section S4) (10–13), and (vi) a nonlinear coherent growth phase upon exceeding a critical threshold (10–13).

To address the above issues, and profiting from the principle of universality in statistical physics, we introduce and study here a semiclassical many-body system in active nanophotonics that exhibits all characteristics of classical SOC but can be quantum-coherently driven. Specifically, we investigate whether light can exhibit a quantum self-organized phase transition to localization in fluctuating dissipative (2, 3) media where simple cavity effects are absent. Many-body interactions (26, 27) in the driven-dissipative nanostructure considered (Fig. 1) arise from the competition between many photonic modes in the presence of nonlinear gain (Fig. 2 and Materials and Methods) and, as shown later on, are vital for robust localization to emerge. Likewise, quantum effects in this system arise from the presence of a coherent drive Ω_a mixing two quantum states in the active core layer of the system (Fig. 1 and section S3), leading to their quantum-coherent superposition—similar to quantum critical systems (for example, ferromagnets) in condensed matter where the application of a classical magnetic field realigns the spins in the direction of the field, leading to a quantum-coherent superposition of "up" and "down" spins (for example, $|\rightarrow\rangle_i = (|\uparrow\rangle_i + |\downarrow\rangle_i)/\sqrt{2}$), that is, to a "quantum paramagnet" (21–25).

Localization in optics and photonics is usually achieved by using a barrier (optical potential) to confine light, for example, in microstructured dielectric cavities or plasmonic nanoparticles and metamaterials. In all cases, this type of localization is thus known as "potential localization" (28–30): The light wave is localized, owing to the sheer presence of a refractive index barrier, without any phase transition occurring. Most existing light localization active structures (such as, for example, optical microcavity or photonic crystal lasers, light-emitting diodes, and modulators) normally involve intricate optogeometric configurations, are

[1]National Science Foundation Nanoscale Science and Engineering Center, University of California, Berkeley, CA 94720, USA. [2]Materials Sciences Division, Lawrence Berkeley National Laboratory, Berkeley, CA 94720, USA.
*These authors contributed equally to this work.
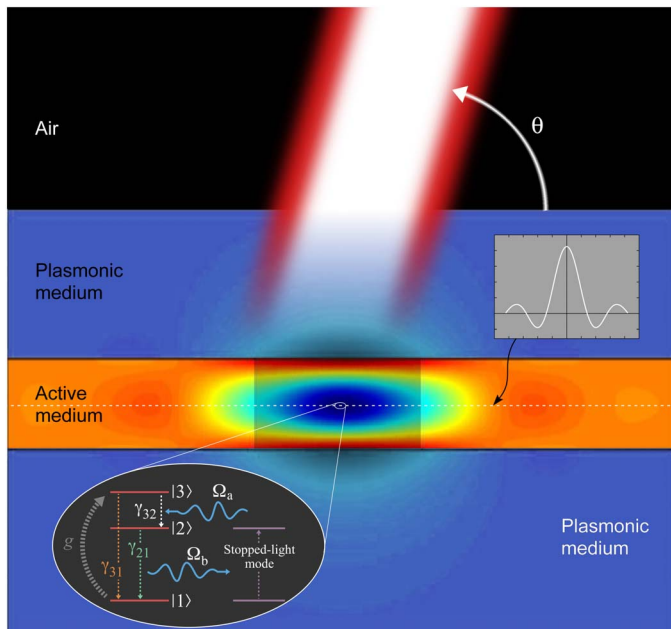†Corresponding author. Email: xiang@berkeley.edu

Fig. 1. The conceived coherence-driven photonic nanosystem. The nonequilibrium system we consider is a quantum-coherently driven active nanophotonic heterostructure in its stopped-light regime. It consists of a 26-nm-thick quantum well (QW) bounded by aluminum (Al), with the upper cladding having a thickness of 50 nm. The QW is described by a three-level scheme (57), as shown in the lower inset. An incoherent incident pump (shown in red) sends electrons from level |1> to level |3> with a pump rate g, whereas a coherent drive (shown in white) couples the levels |2> and |3> with a Rabi frequency Ω_a. Photons emitted in the |2>-|1> transition stimulate coherently the stopped-light ("heavy photon") mode that the heterostructure supports (see Fig. 4). The pump beam deposits gain over the middle region highlighted translucently. Numerical Maxwell-Bloch-Langevin computations (61, 62) reveal the emergence of a sinc-shaped nonequilibrium-localized light field (shown in false color), in agreement with theory (see Fig. 2B, right).

difficult to integrate with waveguides and further multiplexing, and are not CMOS (complementary metal-oxide semiconductor)–compatible nor suitable for scalable, high-volume fabrication (for example, often requiring the creation of air bridge structures or fabrication using electron beam lithography, which is an accurate but time-consuming process) (29). Thus, it is desirable from a technological perspective to design light-localizing structures that can, ideally, be in the form of planar heterostructures, fully compatible with integrated CMOS platforms (for example, suitable for stepper photolithography), and minimalistic—not requiring the fabrication of well-defined longitudinal mirrors/boundaries to confine light. Furthermore, until now, the only known nonpotential light localization mechanism is the Anderson transition in strongly disordered media (28–32) where in three dimensions an equilibrium phase transition occurs from diffusion to exponential localization. However, the so-attained nonpotential light localization is not robust: Dissipative losses (33, 34), nonlinear photon interactions, or time-varying refractive indices (32) can all destroy localization and restore diffusion (see also section S1) (28, 30, 32).

Here, we report on a coherence-driven photonic nanosystem that can dynamically localize light far from thermodynamic equilibrium (35) by interfering many nonlinearly coupled photonic modes in the presence of gain. In sharp contrast to conventional light localization schemes, this is achieved in the absence of refractive index barriers (non–potential-well localization); that is, there is a phase transition

to localization—similarly to the Anderson scheme. However, although there is a phase transition to localization in both our case and the Anderson configuration, our scheme is inherently different: It does not involve disordered media but longitudinally uniform, active plasmonic heterostructures; thus, the localization mechanism here fundamentally differs from that in disordered media (where coherent backscattering by disorder leads to destructive interference of waves returning to points in the medium along time-reversed paths). Furthermore, unlike the Anderson scheme, the attained localization in our case is robust to the simultaneous presence of dissipation, many-body nonlinear interactions, and time-varying media parameters. In this quantum-coherently driven, nonequilibrium configuration, we observe all six of the previously outlined characteristics that a complex system must have to enter the regime of quantum SOC. Moreover, we identify a supercritical region in the phase diagram that is inaccessible to all classically driven SOC systems, emerging only if quantum effects drive the SOC nanosystem.

We note that a variety of light-based many-body systems (36), as well as of open, driven-dissipative quantum systems (37), have been reported in the past, such as cold atomic ensembles and quantum gases in optical cavities (38), arrays of nonlinear cavities and superconducting circuits (enabling quantum simulators) (39, 40), and exciton-polaritons in semiconductor microcavities (41, 42), to name only a few. These systems exhibit a rich variety of dissipative, nonequilibrium dynamics [for example, described by a dissipative Gross-Pitaevskii equation (41)] or even quantum phase transitions such as, for example, open-system realizations of the Dickie quantum phase transition (38). However, these systems typically do not exhibit classical or quantum SOC because they do not fulfill one or more of the aforementioned six general characteristics (10–13) of this type of phase transitions. In particular, those systems typically require precise tuning of a range of parameters, such as, for example, the pumping strength of a far-detuned laser beam, atomic detuning, cavity detuning, atom-field coupling strength, etc., without which dynamical instabilities are prevented. Even with the right choice of parameters, those systems typically exhibit self-organization (rather than SOC), similar to Bénard cell convection or to pattern formation far from equilibrium (2, 3, 8, 9), such as polarization gratings induced by intense femtosecond light irradiation of amorphous materials (42), involving system-wide processes that operate with long-range interactions, rather than statistically independent events (avalanches) arising from next-neighbor interactions (11–13). For the above reasons, those systems are not classified as SOC in the pertinent literature. In contrast, as shown here in the following, our quantum-coherently driven light-localizing nanophotonic system inherently exhibits all generic characteristics of SOC systems, and for a judicious choice of parameters, it may also be possible for the system to enter the previously described regime of quantum SOC.

RESULTS
The quantum-coherently driven complex nanosystem
To see how robust nonpotential light localization and quantum coherence–driven SOC can arise, consider an active nanophotonic heterostructure, as shown in Fig. 1. It consists of a deep–ultraviolet (UV) QW [for example, AlGaN/AlN (43, 44)] bounded on both sides by a nanoplasmonic medium, Al (45, 46). The active nonlinearities in the QW allow for many-body interactions among the supported photonic states (Fig. 2) (27), whereas the nanoplasmonic layers (47) provide, in the stopped-light regime, the positive-feedback mechanism necessary for the system to reach criticality in a self-organized manner without
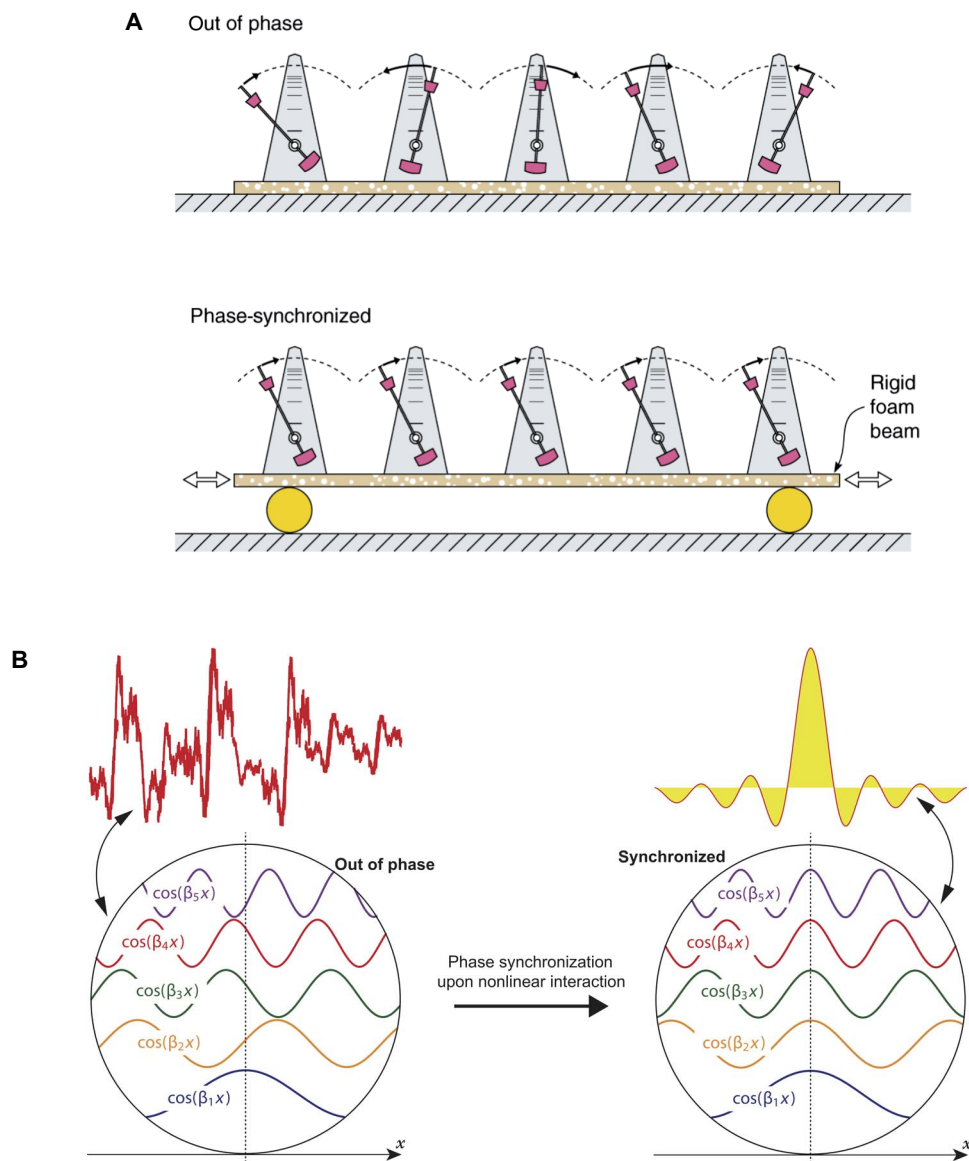
Fig. 2. Synchronization in classical mechanics and in optics. (**A**) The dynamics and emergence of synchronization in many-body classical systems can be modeled using coupled mechanical oscillators (metronomes) (*16*). When a collection of metronomes is placed on a fixed basis (top), in which case they do not couple, they oscillate randomly ("disordered phase"), never synchronizing. In contrast, when the metronomes are placed on a basis that can freely move (bottom), in which case the metronomes couple, they eventually synchronize without any external intervention (that is, "spontaneously"), reaching an "ordered" state where they all move in phase. (**B**) In the active nanophotonic heterostructure that we study (Fig. 1), a large number of oscillating lasing modes couple nonlinearly in the gain region (translucent in Fig. 1) just as the metronomes of (A) couple nonlinearly via the moving base. Each lasing mode can be considered a "particle" in a many-body nonequilibrium system (*27*) and, on its own, is delocalized, oscillating in space with a spatial frequency β_n ($n = 1, 2,...$) (left). These $\{\beta_n\}$ modes initially oscillate out of phase, giving rise to a noise pattern resulting from their superposition and interference (left). However, owing to their nonlinear coupling, they eventually synchronize in space after a transient time interval, giving rise to the emergence of a localized sinc function–shaped supermode (right). The onset of spatial synchronization of the $\{\beta_n\}$ modes is associated with a nonequilibrium first-order phase transition (see main text and Materials and Methods).

the presence of an actual optical potential in the longitudinal direction (see also section S1).

In our analysis of this complex system, we first need to determine an accurate expression for the macroscopic permittivity of the Al layers, $\varepsilon_{Al}(\omega)$, and for this, we first focus on the electron-electron interactions (*26*) in the cover and substrate regions. In Materials and Methods, we present the details of the derived many-electron description of the polarization process in the above layers in the deep-UV regime. We find excellent agreement between experimentally extracted data for the per-

mittivity of Al, $\varepsilon_{Al}(\omega)$, from Ehrenreich *et al.* (*46*) and a fit using our analytically derived expression, verifying the accuracy of this description of the deep-UV plasmonic medium. Note from Fig. 3 that the standard Drude theory fails to predict Re$\{\varepsilon_{Al}(\omega)\}$ < 0 for ω > ~13 × 10^{15} rad/s and, in particular, in the deep-UV region, Re$\{\omega\}$ ~ 16.8 × 10^{15} rad/s, which is the region of interest to us here.

Next, we calculate the complex frequency (*48*, *49*) (complex ω) photonic states that the heterostructure supports (see Materials and Methods). Figure 4 presents an example of such a complex band
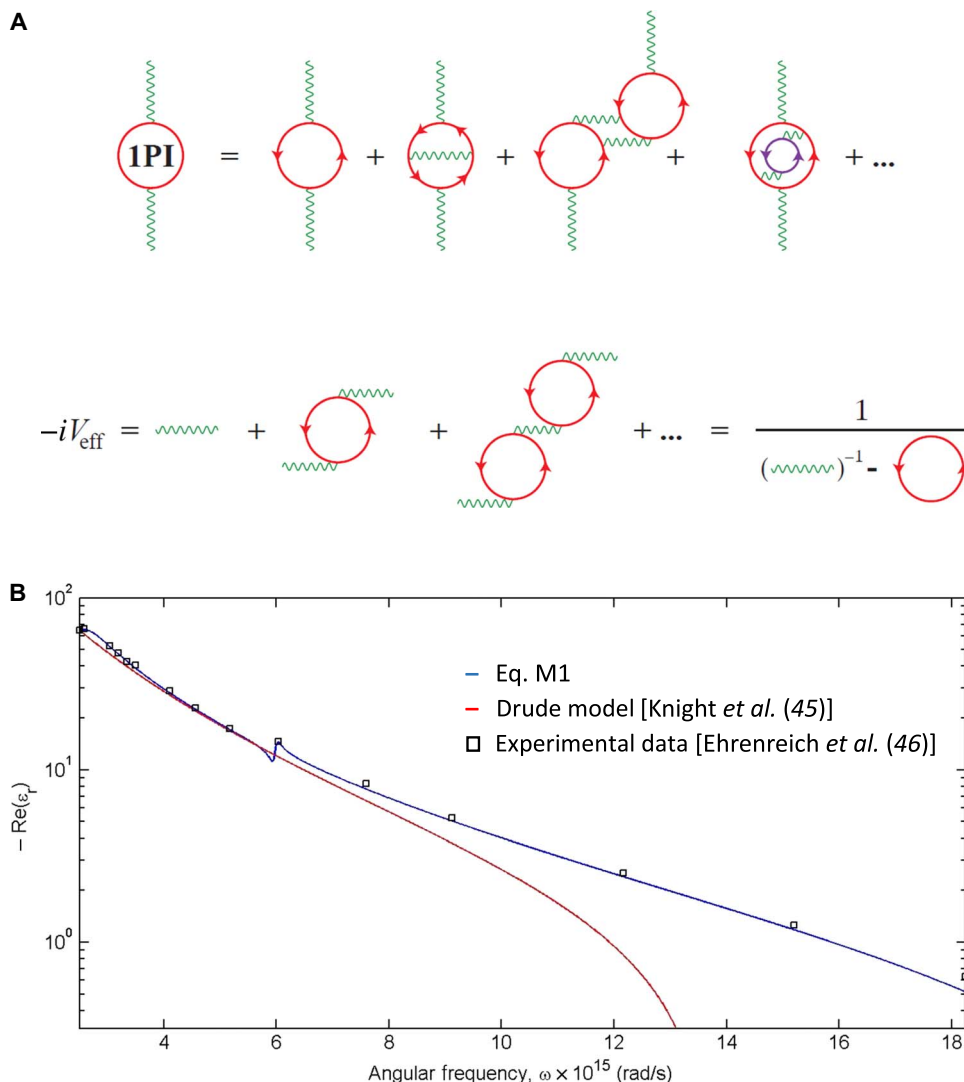
A

B

Fig. 3. Many-electron characteristics of the nanoplasmonic layers of the structure of Fig. 1. (**A**) Feynman diagrams illustrating schematically the polarization process (top) and renormalization of the electron-electron interaction strength, V_e, to V_{eff} (bottom) in the considered plasmonic medium (Al). 1PI, one-particle irreducible. (**B**) Comparison between the real part of the macroscopic permittivity of Al ($-\text{Re}\{\varepsilon_{Al}\}$), as derived from the microscopic theory presented here (Eq. M1), the experimental data by Ehrenreich *et al.* (*46*), and the standard Drude formula (*45*).

structure calculation for the TM_2 photonic mode, showing the real and imaginary parts of the angular frequency ω as a function of the (real) longitudinal propagation constant β. Note from Fig. 4 (bottom) that there are two points, one at $\beta = 0$ and a second at $\beta \sim 30 \times 10^6$ m^{-1}, where the group velocity $v_g \to 0$, making the band very flat for $\beta < 40 \times 10^6$ m^{-1} and inducing a large effective mass of the photonic states in that region ("heavy photons").

We now pump a small region of the active nanoplasmonic heterostructure with a Gaussian incident beam (white beam in Fig. 1), depositing sufficient gain to exceed the dissipative losses (given by Im$\{\omega\}$ in Fig. 4) throughout the $\{\beta \in \mathbb{R}: \beta < 40 \times 10^6$ m$^{-1}\}$ TM_2 band, indicated with a dashed colored circle in the dispersion diagram of Fig. 4. Each β_n point in that part of the band may now become a lasing state (an optical oscillator) (*50*, *51*), with all of them coupling nonlinearly in the gain region where they overlap spatially; that is, we have a many-body system made of a continuous ensemble of coupled optical nano-oscillators, similar to the prototypical SOC model of

coupled mechanical oscillators (see Fig. 2) (*16*). The optical oscillators are not identical here because, although they have nearly the same oscillating frequency ω (because the band is flat in the above $\{\beta\}$ region), they have slightly different losses (red dashed curve in Fig. 4). Nonetheless, we find below, in Fig. 5A, that all $\{\beta\}$ states become unstable and spatially synchronize, similar to the synchronization in time of the metronomes of Fig. 2A (bottom).

To clearly see the emergence of positive feedback in our structure, without which the system cannot reach criticality in a self-organized way, we visualize in Fig. 4 (bottom) the trajectory of a guided light ray in that regime by calculating analytically (section S2) the total time-averaged power flow in the structure. This gives the following compact expression: $P_{tot} = (1/4)E_x^{max}H_y^{max}w_{eff}$, where E_x^{max} (H_y^{max}) is the maximum value of the E_x field (H_y field) component in the core layer, and w_{eff} is the effective thickness of the heterostructure. In the region where the TM_2 band in Fig. 4 is flat and v_g approaches zero, P_{tot} must also approach zero (*52*, *53*) so that $w_{eff} \to 0$; that is, a light
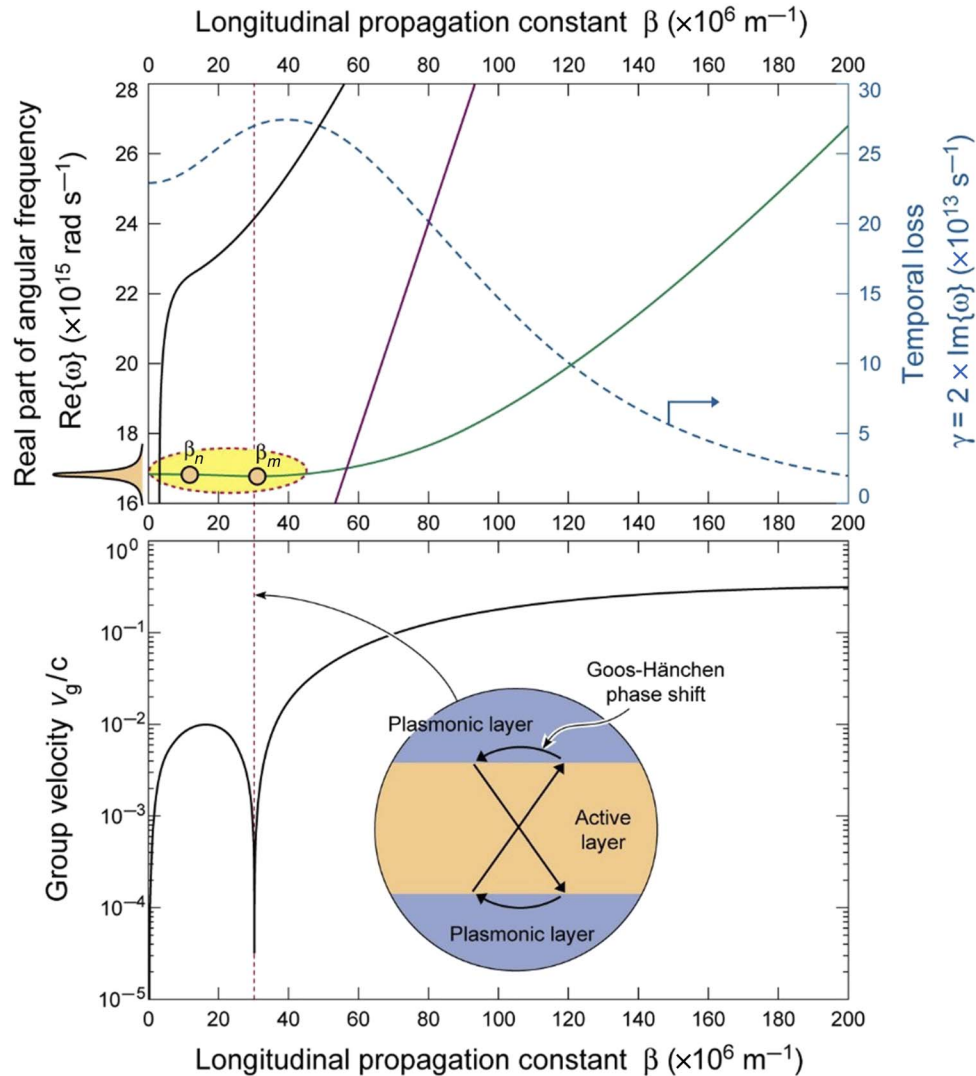
Fig. 4. Complex band diagram of the nanophotonic heterostructure. Complex frequency dispersion band of the TM$_2$ mode. Also shown schematically in the upper panel with a filled Lorentzian shape is the bandwidth of the QW gain (57), whereas highlighted are the excited {β$_n$} states. The lower panel shows the group velocity v_g of the TM$_2$ mode, which becomes zero at two points in the region where β < 40 × 10^6 m^{-1}. The inset in the lower panel presents an intuitive ray picture understanding of how positive feedback arises in the considered self-organized complex nanosystem.

ray becomes trapped, forming a double light cone, as illustrated in the lower inset of Fig. 4. This feedback-forming mechanism is crucial for filtering out of out-of-phase fluctuations and the emergence of robust attractors, as we see below.

Semiclassical mean-field model

We ascertain the regime of quantum coherence–assisted SOC on the basis of a semiclassical mean-field model. We apply a coherent driving field Ω_a (red beam in Fig. 1) to the transition |2⟩ → |3⟩ of the three-level active core medium (QW) (54–58), as shown in the inset of Fig. 1. This creates an asymmetry between absorption and stimulated emission on the |2⟩ → |1⟩ transition and maintains the quantum coherence on the |2⟩ → |3⟩ transition. In contrast, the role of the incoherent pump, g, is simply to excite electrons to the upper state |3⟩, which then decay to states |1⟩ and |2⟩. We design the nanostructure such that the |2⟩ → |1⟩ transition is resonant with the {Re{ω} ≈ 16.8 × 10^{15} rad/s; β ∈ R: β < 40 × 10^6 m^{-1}} TM$_2$ band. The Heisenberg equation of motion for the slowly

varying amplitude $\alpha_{0\beta_n}$ of an individual β$_n$ state is given by (see section S3)

$$\dot{\alpha}_{0\beta_n} = -\Gamma_n \alpha_{0\beta_n} + i\sum_p \rho_{21}^{(p)} \tilde{\Omega}_b^{(p)} \qquad (1)$$

where $|\alpha_{0\beta_n}|^2$ is the number of photons in the mode β$_n$. The decay of excitation of the mode β$_n$ is quantified by the parameter Γ_n, whereas the polarization of the active (gain) medium is given by the nondiagonal matrix elements, such as (section S3)

$$\dot{\rho}_{21} = -\Gamma_{21}\rho_{21} - i\Omega_b(\rho_{22} - \rho_{21}) + i\Omega_a^*\rho_{31} \qquad (2)$$

A key ingredient of Eq. 2 is the presence of the matrix element ρ_{31}, which indicates the coherence between levels |3⟩ and |1⟩ that develops as a result of the coherent drive field Ω_a. This coherence
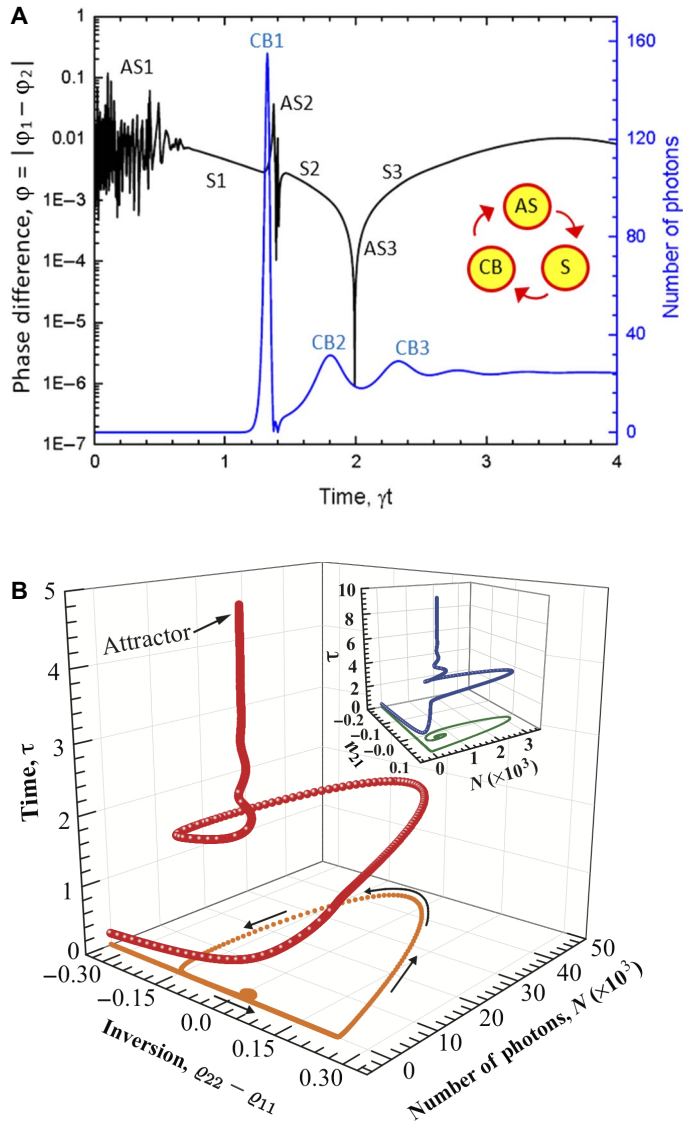
Fig. 5. Spontaneous synchronization and emergence of attractors. (**A**) Onset of synchronization: temporal dynamics of two coupled $\{\beta_n\}$ states showing repeated cycles of asynchronous (AS) motion, followed by synchronization (S), and then temporal coherence buildup (CB). In all cases, the onset of spontaneous synchronization precedes that of activity (CB). (**B**) Emergence of attractors: dynamic evolution in the phase space (control parameter/inversion versus order parameter/photon number) of the localized light field of Fig. 1. After a transient period ($0 < \tau < 3$), during which the light field remains robustly localized and the permittivity of the pumped core region dynamically changes (the control parameter $\rho_{22} - \rho_{11} \propto \text{Im}\{\varepsilon_{co}^{\text{pumped}}\}$), the system is attracted to a stable point, robust to perturbations. The inset shows the same result but without quantum coherence driving the system.

between the atomic states gives rise to quantum interference that is destructive for absorption and constructive for emission processes (55, 56, 58). The electric field associated with $\alpha_{0\beta_n}$ is given by

$$\tilde{E}(z) = i \sum_{n=0}^{N-1} \{2\pi\hbar\omega_n/V\}^{1/2} e^{i[(\beta_1 + n\delta\beta)z + \varphi_n]}\alpha_n^{t=0} - \text{c.c.}\} \qquad (3)$$

where we note that the phases φ_n are different for each mode. Eventually, because of the nonlinear coupling of the β_n modes in the pumped region

(Fig. 1), the modes synchronize as is shown in Fig. 5A, that is, they all obtain the same phase φ_n, which can be set to zero without loss of generality. The supermode arising from the synchronization of all of these modes has a sinc-shaped spatial profile given by (see Materials and Methods)

$$I \propto (2/L_{\text{loc}})^2 \sin c^2(L/L_{\text{loc}}) \qquad (4)$$

where $L_{\text{loc}} = 2/\Delta\beta$ is the localization length. Finally, as shown in Materials and Methods for the present system, but as it is also known for active (lasing) systems in general (50, 51, 55), the control parameter ("effective temperature") in this configuration is the amount of gain in the pumped region, that is, the population inversion $\rho_{33} + \rho_{22} - \rho_{11}$.

From the above discussion, it is thus evident that the succession of elements used in the present model to attain quantum coherence–driven SOC and nonequilibrium light localization is as follows: (i) A pump field deposits gain (population inversion $\rho_{33} + \rho_{22} - \rho_{11}$) in a finite region in the core of the heterostructure (Fig. 1); (ii) the modes β_n destabilize and start oscillating, each with an amplitude $\alpha_{0\beta_n}(t)$ (Eq. 1); (iii) the modes initially oscillate out of phase (Fig. 2B, left) but eventually synchronize (Figs. 2B, right, and 5A), owing to their nonlinear coupling in the gain region; (iv) the synchronization of the modes gives rise to a sinc-shaped localized hotspot (Fig. 1 and Eq. 4); (v) the light intensity in this hotspot is controlled by the population inversion $\rho_{33} + \rho_{22} - \rho_{11}$, which is a function of the coherent field Ω_a (section S3 and Eq. 2); (vi) for a specific value of Ω_a, the critical population inversion $\rho_{33}^c + \rho_{22}^c - \rho_{11}^c$ ["critical temperature" (50, 51, 55) of the system] drops to zero (Fig. 6B), which is a requirement for entering the regime of quantum SOC.

Onset of activity

There is a further crucial point discerned from Fig. 5A: The onset of synchronization is followed in time by the onset of "activity" (59), that is, here, by buildup of temporal coherence (CB), which then destroys synchronization, leading to AS motion (AS2 region in Fig. 5A), followed again by synchronization (S2) and then CB (CB2). We thus have repeated cycles of "AS" motion→leading to "S" motion→leading to "CB"→leading to "AS" motion, until the nonequilibrium steady state is reached. Note that, even at a steady state, this semiclassical many-body (27) nanosystem is still far from thermodynamic equilibrium because the inverted active medium is described by an occupation Boltzmann distribution function with a negative effective temperature ($T_{\text{active-medium}} < 0$), whereas the nanostructure has a temperature much smaller than $\hbar\omega/k_B$ (k_B being Boltzmann's constant); hence, we may effectively put $T_{\text{nanostructure}} \approx 0$. Thus, the light field is coupled to two reservoirs with very different temperatures, and for this reason, the complex nanosystem is far from thermal equilibrium. Note also that, similar to the sandpile cellular automaton SOC model (10, 15), where although the current of incoming particles is known, the control parameter (slope increase of the sandpile) varies randomly and does not require external fine-tuning, also in our case, although the pump rate may be known, the control parameter [atomic inversion (v)] cannot be precisely known or tuned, owing to spontaneous emission; in both cases, the complex system is automatically attracted to the nonequilibrium self-organized critical point (Fig. 5B and Materials and Methods).

The evolution in the phase space of the robustly (and nonpotentially) localized hotspot, which, as we saw, arises from the superposition of all $\{\beta\}$ states, is reported in Fig. 5B, showing the emergence of a steady-state
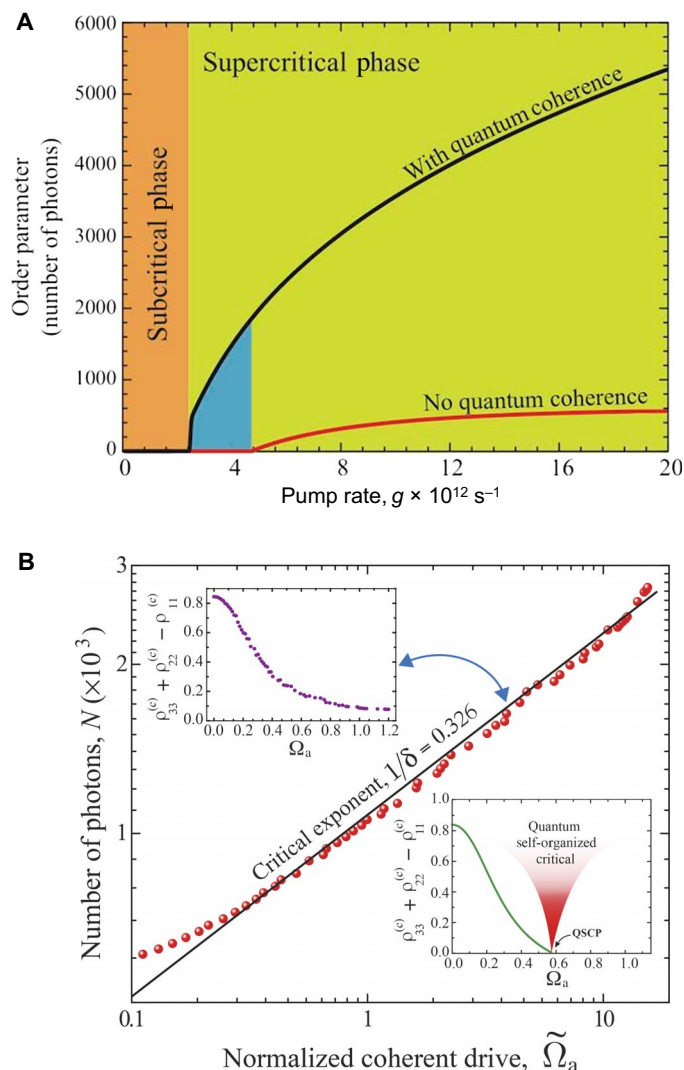
Fig. 6. Emergence of scaling and toward the quantum self-organized critical regime. (A) Order parameter (number of photons) versus the pump rate, g, with and without quantum coherence driving the nanosystem. The nonlinearly interacting $\{\beta_n\}$ lasing modes self-organize into a critical state, with a second-order (first-order) phase transition to a supercritical phase being observed without (with) the quantum-coherent drive. **(B)** Emergence of scale-invariant (fractal) power law in the order parameter versus the normalized coherent drive $\tilde{\Omega}_a = \Omega_a/(\rho_{33}^c + \rho_{22}^c - \rho_{11}^c)$, where $\rho_{33}^c + \rho_{22}^c - \rho_{11}^c$ is the critical inversion. The computed critical isotherm exponent is $\delta \sim 3.07$. The upper inset shows the variation of the critical inversion with the applied coherent field Ω_a. For another suitably selected choice of parameters (see section S3), the control parameter (that is, the critical inversion $\rho_{33}^c + \rho_{22}^c - \rho_{11}^c$, which plays the role of the effective temperature here) reduces to zero for a sufficiently strong drive Ω_a (lower inset). That point is the quantum self-organized critical point (QSCP) of our nonequilibrium dynamical system, somewhat analogous to the quantum critical point (QCP) in equilibrium static systems in condensed matter (21–25).

nonequilibrium attractor, robust with respect to noise; that is, the self-organized critical point becomes an attractor for the dynamics. Note also from Fig. 5B the marked evolutionary advantage of the quantum coherence–driven complex nanosystem compared with the case where the system is only classically driven (inset in Fig. 5B): First, steady state is reached faster, and second, the number of photons generated, that is, the

intensity of the nonequilibrium-localized hotspot, increases by more than an order of magnitude.

DISCUSSION
To better observe the effect of the coherent control on the considered nonequilibrium nanosystem, we have derived and show in Fig. 6A its phase diagram, both with and without the external coherent drive. Note how the continuous, second-order phase transition in the absence of quantum coherence is transformed to a discontinuous first-order phase transition when the coherent field drives the SOC nanosystem. We find from Fig. 6A that the presence of quantum coherence not only preserves but also actually enhances SOC: The magnitude of the order parameter markedly increases under the quantum-coherent drive, and furthermore, there is a region (highlighted with pale blue in Fig. 6A) that was subcritical in the absence of quantum coherence but becomes supercritical in the presence of quantum coherence.

Finally, Fig. 6B presents two of the key results of the present study: First, similar to classical SOC systems (15), we find (in mean-field approximation) that the order parameter obeys a scale-invariant power law as a function of the normalized quantum-coherent drive $\tilde{\Omega}_a$ with a "critical isotherm" (14, 50, 51, 55) exponent $\delta \sim 3.07$. Our quasi-1D system belongs to the Ising universality class, but unlike equilibrium static systems in condensed matter, here, the critical point is reached by starting far from thermodynamic equilibrium in a self-organized manner. The presence of an attractor in Fig. 5B is insensitive to the parameters of the model. This robustness to dissipation, fluctuations, and many-body interactions is the fundamental difference of the present type of nonpotential light localization compared to light localization in disordered media. Second, similar to quantum criticality in equilibrium static systems, which is reached when the critical temperature T_c drops to zero upon application of an external magnetic field (21–23), the lower inset of Fig. 6B shows that, for a suitable choice of parameters (section S3), the effective critical temperature of our nonequilibrium dynamical system falls to zero for sufficiently strong coherent drive ($\Omega_a \sim 0.6$). Exactly that point, where the total critical inversion $\Delta\rho_c$ (critical effective temperature; see Materials and Methods) falls to zero, is a quantum self-organized critical point, analogous to the quantum critical point in equilibrium phase-transition phenomena (compare Fig. 1) (21–24) but without the need for fine-tuning.

In conclusion, the main findings of the present study can be summarized as follows: First, we have identified a quantum coherence–driven self-organized phase transition in an active nanophotonic system (Figs. 1 and 4B). Second, we have shown that quantum coherence bestows a marked advantage in the evolution of self-organized systems toward a phase transition; namely, it accelerates the reaching of the critical point (Fig. 5B) and enhances the order parameter (Fig. 6A). Third, we have identified a scheme where unconventional light localization is attained: Similar to the Anderson scheme in disordered media, there is phase transition to localization (that is, the localization is not trivial because it is not aided by cavity-like effects); however, unlike the Anderson scheme, we do not deploy disordered media (but active, longitudinally uniform, plasmonic heterostructures), and the attained dynamical localization remains unharmed by and robust to dissipative effects, nonlinear many-body interactions, and time-varying media parameters (Figs. 2B and 5). The fact that there is no need to design optical potentials in this scheme for robustly localizing light [that is, the fact that the conceived nanostructure is minimalistic (planar and longitudinally uniform)] strongly suggests that it is also appealing

from an applied perspective for a host of applications in condensed matter photonics and nanophotonics.

MATERIALS AND METHODS
Many-electron polarization process in the cover and substrate layers

The response of the electron gas to a spatiotemporally varying weak potential $V_e(\mathbf{r}, t) = V_e(\mathbf{q}, \omega)e^{i(\mathbf{qr}-\omega t)}e^{\gamma t}$ ($\gamma \to 0$) is governed by the Hamiltonian (26) $H = \sum_{\mathbf{p},s}\varepsilon_{\mathbf{p}}\hat{a}_{\mathbf{p}s}^{+}\hat{a}_{\mathbf{p}s} + \sum_s \int \hat{\Phi}_s^{+}(\mathbf{r}) V_e(\mathbf{r}, t) \hat{\Phi}_s(\mathbf{r}) d^3r$, where $\varepsilon_{\mathbf{p}} = \hbar^2 k^2/2m$ is the energy of a single-electron state, $\hat{a}_{\mathbf{p}s}^{(+)}$ is the annihilation (creation) operator for a state with wave vector $\mathbf{p}$ and spin s, and $\hat{\Phi}_s^{(+)}(\mathbf{r}) = \frac{1}{V^{1/2}}\sum_{\mathbf{p}}\hat{a}_{\mathbf{p}s}^{(+)}e^{(-)i\mathbf{p}\cdot\mathbf{r}}$ is the corresponding electron field operators. In the Heisenberg representation, the equation of motion of the relevant density operator is, thus, given by $i\hbar\,d(\hat{\rho}_{\mathbf{p},\mathbf{q},s})/dt = (\varepsilon_{\mathbf{p}+\mathbf{q}} - \varepsilon_{\mathbf{q}})\hat{\rho}_{\mathbf{p},\mathbf{q},s} + (\hat{a}_{\mathbf{p},s}^{+}\hat{a}_{\mathbf{p},s} - \hat{a}_{\mathbf{p}+\mathbf{q},s}^{+}\hat{a}_{\mathbf{p}+\mathbf{q},s})V_e(\mathbf{q},\omega)$ from where upon taking the thermal average ($<\hat{Q}> = \mathrm{Tr}(\hat{Q}e^{-\beta H})/Z$, β being the thermodynamic beta, and Z being the canonical partition function), we found the dynamical response function $\chi_0(\mathbf{q}, \omega) = (1/V)\sum_{\mathbf{p},s}(n_{\mathbf{p}+\mathbf{q},s}^0 - n_{\mathbf{p},s}^0)/(\varepsilon_{\mathbf{p}+\mathbf{q}} - \varepsilon_{\mathbf{q}} - \hbar\omega - i\hbar\gamma)$, where $n_{\mathbf{p},s}^0 = <\hat{a}_{\mathbf{p},s}^{+}\hat{a}_{\mathbf{p},s}>$. For the polarization process in the plasmonic medium, we needed to sum all one-particle irreducible Feynman diagrams that can be inserted into an interaction wiggle [an example of which (for $i\chi_0$) is shown in Fig. 3A]. In the absence of a photon propagator at this stage, the aforementioned sum will simply renormalize the potential, changing the interaction strength from $-iV_e$ to the effective potential $-iV_{\mathrm{eff}}$. Carrying out the sum to infinity in the usual way (see Fig. 3A), we got $-iV_{\mathrm{eff}} = -iV_e + (-iV_e)(i\chi_0)(-iV_e) + (-iV_e)(i\chi_0)(-iV_e)(i\chi_0)(-iV_e) + \ldots = (-iV_e)/(1 - V_e\chi_0)$, from where the equivalent permittivity may be defined as $\varepsilon(\mathbf{q}, \omega) = 1 - V_e\chi_0 = 1 - 4\pi e^2\chi_0(\mathbf{q},\omega)/q^2$. Here, we sought to identify the smallest possible nanovolume over which nonequilibrium light localization of oscillatory (that is, not surface) states may be achieved in the considered Al nanoplasmonic heterostructure; hence, we needed to consider the highest possible incident light frequencies (in this case, in the deep-UV regime), for which not only conduction band (that is, sp band) but also d band to sp band electronic transitions are important. In particular, Al (and other non-noble metals) contains multiple valence electrons that, for the high-energy deep-UV incident photons that we shall consider here, can transition between parallel or near-parallel one-electron conduction bands (sp band to sp band). Thus, assuming that $|\mathbf{q}| \ll k_F$ (k_F being the radius of the Fermi sphere in k space around $\mathbf{k} = 0$), expanding $\chi_0(\mathbf{q}, \omega)$ in $\mathbf{q}$, taking into account that $\varepsilon_{\mathbf{p}+\mathbf{q}} = \varepsilon_{\mathbf{p}} + \mathbf{q}\cdot\nabla_{\mathbf{p}}\varepsilon_{\mathbf{p}}+\ldots$, $n_{\mathbf{p}+\mathbf{q}}^0 = n_{\mathbf{p}}^0 + (\partial n^0/\partial\varepsilon)\mathbf{q}\cdot\nabla_{\mathbf{p}}\varepsilon_{\mathbf{p}} + \ldots$, and $\partial n^0/\partial\varepsilon_{\mathbf{p}} = -\delta(\varepsilon_{\mathbf{p}} - \varepsilon_F)$ (at $T = 0$), with $\nabla_{\mathbf{p}}\varepsilon_{\mathbf{p}} = \hbar v_F\mathbf{k}/k$ being the Fermi velocity, and using standard second-order perturbation theory, we arrived at the following generic expression for the nonnoble metal (Al) dynamic permittivity

$$\varepsilon_{\mathrm{Al}}(\omega) = \lim_{|\mathbf{q}|\to 0}\varepsilon(\mathbf{q}, \omega) -$$

$$\frac{4\pi i e^2}{\omega m^2}\sum_{i,j}\frac{f(E_i) - f(E_j)}{E_i - E_j}\frac{<i|p_a|j><j|p_b|i>}{-i\omega + 1/\tau + (i/\hbar)(E_i - E_j)} \quad (M1)$$

where the sum is over the valence and conduction band states i and j, $f(E_i)$ and $f(E_j)$ are the Fermi functions (appearing owing to the Pauli principle), "a" is the direction upon which the current density flows upon application of an electric field in the direction "b," τ is the relaxation time, and $< i \mid p_a \mid j >$ is the magnitude of the momentum matrix element coupling the valence band state i and the conduction band state j. Figure 3B reports an excellent agreement between experimentally extracted data for $\varepsilon_{\mathrm{Al}}(\omega)$ by Ehrenreich et al. (46) and a fit using Eq. M1 above, verifying the accuracy of the above many-electron theory.

Transfer matrix and argument principle methods

Assuming that a light wave in the i-th layer oscillates as $\varphi_i^1\cos[\kappa_i(x - x_{i-1})] + \varphi_i^2(u_i/\kappa_i)\sin[\kappa_i(x - x_{i-1})]$, with $u = \varepsilon_i(\mu_i)$ for transverse magnetic (transverse electric) modes and that the light wave in the terminating Nth layer is of the form $\alpha_N e^{\gamma_N(x - x_N)}$, the photonic states obey a general dispersion relation of the form (48) $F(\omega, \beta^2) = \varphi_N^2 - \varphi_N^1(\gamma_N/u_N) = 0$, where $\gamma_N = (\beta^2 - k_0^2 n_N^2)^{1/2}$, β being the longitudinal propagation constant, k_0 being the vacuum wave number, and φ_N^1 and φ_N^2 being the oscillatory wave constants. The M roots, w, of the (analytic) function F in a bound domain K with smooth boundary ∂K can be found using the argument principle method (APM), according to which $\frac{1}{2\pi i}\oint_{\partial K}w^{\ell}\frac{F'(w)}{F(w)}dw = \sum_{i=1}^{M}w_i^{\ell}$, with ℓ being a positive integer. The number of roots in the domain K is identified by setting $\ell = 0$. Upon isolation of a root, we may set $\ell = 1$ to locate its exact position on K. For the applicability of the APM, the complex function $F(\omega, \beta^2)$ must be analytic and without poles in the domain K; however, in its above form, $F(\omega, \beta^2)$ has two branch points at $\beta^2 = k_0^2 n_1^2$ and $\beta^2 = k_0^2 n_N^2$, resulting in a four-sheeted Riemann surface [where, for a given value of β^2, $F(\omega, \beta^2)$ takes on four possible values]. To unfold the four-sheeted Riemann surface (β^2 plane) and map it onto a new complex variable z ($H(z) = F[\xi(z)]$, with ξ representing the original complex solution plane that is mapped onto the new complex variable z), we introduced two functions, $g(z)$ and $h(z)$, demanding that $g^2(z) = \beta^2 - \xi(z)n_1^2$ and $h^2(z) = \beta^2 - \xi(z)n_N^2$, which can also be written as $g(z) = n_1(e^z + Re^{-z})$ and $h(z) = n_N(e^z - Re^{-z})$, where $R = \beta^2(n_N^2 - n_1^2)/(4n_N^2 n_1^2)$; hence, $\xi(z) = S - e^{2z} - R^2 e^{-2z}$, with $S = \beta^2(n_N^2 + n_1^2)/(2n_N^2 n_1^2)$, from where the angular frequency may be calculated as $\omega(z) = c[\xi(z)]^{1/2}$.

First-order phase transition to synchronization of the $\{\beta_n\}$ states

The synchronization in space (rather than only in time) of the $\{\beta_n\}$ states shown in Figs. 2B and 5A, leading to robust nonpotential localization, is a first-order phase-transition phenomenon arising from their nonlinear coupling. To better observe this, we started by considering the general equation governing the coupling between the field amplitudes α_n in the presence of dispersion and nonlinearity (27, 60) $\dot{\alpha}_n = (\chi_n - \xi_n - i\delta_n)\alpha_n + (\upsilon_{\mathrm{sat}} + i\upsilon_{\mathrm{nonl}})\sum_{p-p'+q=n}\alpha_p\alpha_{p'}^*\alpha_q + SF_n$, where χ_n is the gain at the frequency of the β_n state, δ_n is the phase accumulated over a cycle (associated with group-velocity dispersion), υ_{sat} is associated with the saturable amplitude, and υ_{nonl} is associated with the third-order nonlinearity. The frequency-dependent gain saturation may, as usual, be modeled by $\chi_n = \chi_{0,n}/\left(1 + \sum_n \chi_{0,n}\alpha_n\alpha_n^*/\sum_n \chi_{0,n}^{\mathrm{sat}}\alpha_n^{\mathrm{sat}}\alpha_n^{\mathrm{sat}*}\right)$, where the constant $\sum_n \chi_{0,n}^{\mathrm{sat}}\alpha_n^{\mathrm{sat}}\alpha_n^{\mathrm{sat}*}$ term represents the saturation power. It is now a simple exercise to show that the field amplitudes α_n obey, equivalently, the equation $\dot{\alpha}_n = -i\partial H'/\partial\alpha_n^* - \partial H''/\partial\alpha_n^* + SF_n$, where $H' = -\upsilon_{\mathrm{nonl}}\sum_{p-p'+q=n}\alpha_p\alpha_{p'}^*\alpha_q\alpha_n^* - \sum_n \delta_n\alpha_n\alpha_n^*$

and $H'' = -\upsilon_{\text{sat}} \sum\limits_{p-p'+q=n} \alpha_p \alpha_{p'}^* \alpha_q \alpha_n^* + \sum\limits_n \xi_n \alpha_n \alpha_n^* - \sum\limits_n \chi_{0,n}^{\text{sat}} \alpha_n^{\text{sat}} \alpha_n^{\text{sat}*}$

$\ln\left(\sum\limits_n \chi_{0,n}^{\text{sat}} \alpha_n^{\text{sat}} \alpha_n^{\text{sat}*} + \sum\limits_n \chi_{0,n} \alpha_n \alpha_n^*\right)$. From Fig. 4, we can see that the {β} band is very flat (that is, the group-velocity dispersion is negligible), and hence, we may put $\delta_n = 0$. Furthermore, if we assume that the effect of self-phase modulation is inconsequential ($\upsilon_{\text{nonl}} = 0$) here, we may immediately recognize from the above expression for α_n that $-H''$ can be associated with the Gibbs free energy, G. Upon expanding the logarithmic term in H'' to second order, we may therefore arrive at the following expression for G: $G = \sum\limits_n \left(\xi_n - \chi_{0,n} - \psi_{\text{sat}} \sum\limits_n \chi_{0,n}^{\text{sat}} \alpha_n^{\text{sat}} \alpha_n^{\text{sat}*}\right)$

$\alpha_n \alpha_n^* + \left(\frac{1}{2\sum\limits_n \chi_{0,n}^{\text{sat}} \alpha_n^{\text{sat}} \alpha_n^{\text{sat}*}} - \upsilon_{\text{sat}}\right) \sum\limits_{p-p'+q=n} \alpha_p \alpha_{p'}^* \alpha_q \alpha_n^*$, where $\psi_{\text{sat}} = \ln\left(\sum\limits_n \chi_{0,n}^{\text{sat}} \alpha_n^{\text{sat}} \alpha_n^{\text{sat}*}\right)$. This expression for G is very similar to the Landau expression for the free energy of a system spontaneously undergoing a first-order phase transition: The coefficient of the second-order term ($\alpha_n \alpha_n^*$) can become negative for high values of the gain ($\chi_{0,n}$), signifying the onset of spontaneous symmetry-breaking, and for high values of the nonlinear saturable amplitude, υ_{sat}, the coefficient of the fourth-order term of G is also negative, thereby describing a first-order phase transition.

Emergence of sinc-shaped localized hotspot

As seen from Fig. 5A, initially, two quantum-coherently driven β_n states are completely AS, but they eventually synchronize, owing to their nonlinear coupling in the pumped active region—similar to the eventual synchronization of the motion of the pendulum metronomes in Fig. 2A. As has just been demonstrated analytically above, the onset of synchronization is associated here with a nonequilibrium first-order phase transition, with the role of temperature played by the atomic inversion (50, 51). The instantaneous electric field along z at an arbitrary time instant $t = 0$ is given by the superposition of all β_n states $\tilde{E}(z) = i \sum\limits_{n=0}^{N-1} \{2\pi\hbar\omega_n / V\}^{1/2} e^{i[(\beta_1 + n\delta\beta)z + \varphi_n]}$ $\alpha_n^{t=0} - \text{c.c.}\}$ and is initially (before synchronization) a noise signal because φ_n is different for each β_n state (Fig. 2B, left). To see how a nonrandom localized field pattern emerges upon synchronization ("optical morphogenesis"), we calculated $\tilde{E}(z)$ at a later time instant $t = t'$ at which the fields at a point $z = L$ oscillate coherently, that is, $\varphi_n = \varphi = 0, \tilde{E}(z = L) = A \sum\limits_{n=0}^{N-1} e^{in\delta\beta L} e^{i\beta_1 L} \xrightarrow[\beta_1 = 0, \delta\beta \to 0]{\beta_{\max} = \Delta\beta} A \int\limits_0^{\Delta\beta} e^{i\beta L} d\beta = A(e^{i\Delta\beta L} - 1)/(iL)$. Therefore, in the pumped region, the field intensity of the localized hotspot upon synchronization will be $I \propto E^2 \propto \Delta\beta^2 [(e^{i\Delta\beta L} - 1)/(\Delta\beta L)] \cdot [(e^{-i\Delta\beta L} - 1)/(\Delta\beta L)] = \Delta\beta^2 \text{sinc}^2(\Delta\beta L/2)$, where $\Delta\beta = \beta_{\max} \approx 40 \times 10^6 \text{ m}^{-1}$, which can also be written as

$$I \propto (2/L_{\text{loc}})^2 \text{sinc}^2(L/L_{\text{loc}}) \qquad (M2)$$

with $L_{\text{loc}} = 2/\Delta\beta$ being the localization length.

Note that these expressions for I and L_{loc} are completely independent of the shape and width of the pump and coherent-drive beams because they should be for true localization. The characteristics of the nonequilibrium-localized hotspot depend only on the intrinsic characteristics of the active nanostructure and arise from the interaction and spontaneous synchronization of the β_n states. The flatter the TM_2

band is in the reciprocal space [that is, the more β_n states participate in the cooperative process (that is, the larger the $\Delta\beta$ is)], the "tighter" in space and more intense will the hotspot become. To further corroborate the validity of Eq. M2, Fig. 1 shows a steady-state snapshot from full-wave Maxwell-Bloch-Langevin time domain simulations (61, 62) of the spatial shape of the emergent localized light field, which has a sinc function dependence in the longitudinal direction. Note that this is not a potential localization: It does not arise from jumps in either the real or the imaginary part of the permittivity of the active region (see section S1).

SUPPLEMENTARY MATERIALS

REFERENCES AND NOTES

1. Nature Insight, Complex systems. *Nature* **410**, 241–284 (2001).
2. G. Nicolis, I. Prigogine, *Self-Organization in Nonequilibrium Systems: From Dissipative Structures to Order Through Fluctuations* (Wiley, 1977).
3. I. Prigogine, *Time, Structure and Fluctuations: Nobel Lecture in Chemistry* (Nobel Foundation, 1977).
4. B. Feltz, M. Crommelinck, P. Goujon, Eds., *Self-Organization and Emergence in Life Sciences* (Springer, 2006).
5. J. Buhl, D. J. T. Sumpter, I. D. Couzin, J. J. Hale, E. Despland, E. R. Miller, S. J. Simpson, From disorder to order in marching locusts. *Science* **312**, 1402–1406 (2006).
6. D. Helbing, I. Farkas, T. Vicsek, Simulating dynamical features of escape panic. *Nature* **407**, 487–490 (2000).
7. V. A. Kostelecký, J. Pantaleone, S. Samuel, Neutrino oscillations in the early universe. *Phys. Lett. B* **315**, 46–50 (1993).
8. J. Bard, *Morphogenesis: The Cellular and Molecular Processes of Developmental Anatomy* (Developmental and Cell Biology Series, Cambridge Univ. Press, 1992).
9. A. M. Turing, The chemical basis of morphogenesis. *Philos. Trans. R. Soc. B* **237**, 37–72 (1952).
10. P. Bak, C. Tang, K. Wiesenfeld, Self-organized criticality: An explanation of the 1/f noise. *Phys. Rev. Lett.* **59**, 381–384 (1987).
11. P. Bak, *How Nature Works: The Science of Self-Organised Criticality* (Springer, 1999).
12. H. J. Jensen, *Self-Organised Criticality: Emergent Complex Behavior in Physical and Biological Systems* (Cambridge Lecture Notes in Physics, Cambridge Univ. Press, 1998).
13. M. Aschwanden, *Self-Organized Criticality in Astrophysics: The Statistics of Nonlinear Processes in the Universe* (Springer, 2011).
14. L. P. Kadanoff, W. Götze, D. Hamblen, R. Hecht, E. A. S. Lewis, V. V. Palciauskas, M. Rayl, J. Swift, D. Aspnes, J. Kane, Static phenomena near critical points: Theory and experiment. *Rev. Mod. Phys.* **39**, 395–431 (1967).
15. C. Tang, P. Bak, Critical exponents and scaling relations for self-organized critical phenomena. *Phys. Rev. Lett.* **60**, 2347–2350 (1988).
16. C. Tang, K. Wiesenfeld, P. Bak, S. Coppersmith, P. Littlewood, Phase organization. *Phys. Rev. Lett.* **58**, 1161–1164 (1987).
17. M. H. Ansari, L. Smolin, Self-organized criticality in quantum gravity. *Class. Quantum Grav.* **25**, 095016 (2008).
18. Nature Insight, Quantum coherence. *Nature* **453**, 1003–1049 (2008).
19. N. Lambert, Y.-N. Chen, Y.-C. Cheng, C.-M. Li, G.-Y. Chen, F. Nori, Quantum biology. *Nat. Phys.* **9**, 10–18 (2013).
20. P. Ball, Physics of life: The dawn of quantum biology. *Nature* **474**, 272–274 (2011).
21. S. Sachdev, *Quantum Phase Transitions* (Cambridge Univ. Press, 1999).
22. S. Sachdev, B. Keimer, Quantum criticality. *Phys. Today* **64**, 29 (2011).

23. P. Coleman, A. J. Schofield, Quantum criticality. *Nature* **433**, 226–229 (2005).
24. A. Kopp, S. Chakravarty, Criticality in correlated quantum matter. *Nature Phys.* **1**, 53–56 (2005).
25. R. Coldea, D. A. Tennant, E. M. Wheeler, E. Wawrzynska, D. Prabhakaran, M. Telling, K. Habicht, P. Smeibidl, K. Kiefer, Quantum criticality in an Ising chain: Experimental evidence for emergent E8 symmetry. *Science* **327**, 177–180 (2010).
26. P. Coleman, *Introduction to Many-Body Physics* (Cambridge Univ. Press, 2016).
27. B. Fischer, A. Bekker, Many-body photonics. *Opt. Photon. News* **24**, 40–47 (2013).
28. P. W. Anderson, Absence of diffusion in certain random lattices. *Phys. Rev.* **109**, 1492–1505 (1958).
29. P. Markoš, C. M. Soukoulis, *Wave Propagation: From Electrons to Photonic Crystals and Left-Handed Materials* (Princeton Univ. Press, 2008).
30. P. Sheng, *Introduction to Wave Scattering, Localization and Mesoscopic Phenomena* (Academic Press, 1995).
31. A. Rodriguez, L. J. Vasquez, K. Slevin, R. A. Römer, Critical parameters from a generalized multifractal analysis at the Anderson transition. *Phys. Rev. Lett.* **105**, 046403 (2010).
32. M. Segev, Y. Silberberg, D. N. Christodoulides, Anderson localization of light. *Nat. Photonics* **7**, 197–204 (2013).
33. I. Yusipov, T. Laptyeva, S. Denisov, M. Ivanchenko, Localization in open quantum systems. *Phys. Rev. Lett.* **118**, 070402 (2017).
34. S. Genway, I. Lesanovsky, J. P. Garrahan, Localization in space and time in disordered-lattice open quantum dynamics. *Phys. Rev. E* **89**, 042129 (2014).
35. Nature Physics Insight, Nonequilibrium physics. *Nat. Phys.* **11**, 103–139 (2015).
36. C. Noh, D. G. Angelakis, Quantum simulations and many-body physics with light. *Rep. Prog. Phys.* **80**, 016401 (2016).
37. L. M. Sieberer, M. Buchhold, S. Diehl, Keldysh field theory for driven open quantum systems. *Rep. Prog. Phys.* **79**, 096001 (2016).
38. H. Ritsch, P. Domokos, F. Brennecke, T. Esslinger, Cold atoms in cavity-generated dynamical optical potentials. *Rev. Mod. Phys.* **85**, 553–601 (2013).
39. M. J. Hartmann, Quantum simulation with interacting photons. *J. Opt.* **18**, 104005 (2016).
40. A. A. Houck, H. E. Türeci, J. Koch, On-chip quantum simulation with superconducting circuits. *Nat. Phys.* **8**, 292–299 (2012).
41. D. Sanvitto, S. Kéna-Cohen, The road towards polaritonic devices. *Nat. Mater.* **15**, 1061–1073 (2016).
42. M. Beresna, M. Gecevičius, P. G. Kazansky, T. Taylor, A. V. Kavokin, Exciton mediated self-organization in glass driven by ultrashort light pulses. *Appl. Phys. Lett.* **101**, 053120 (2012).
43. Y. Taniyasu, M. Kasu, T. Makimoto, An aluminium nitride light-emitting diode with a wavelength of 210 nanometers. *Nature* **441**, 325–328 (2006).
44. H. Yoshida, Y. Yamashita, M. Kuwabara, H. Kan, A 342-nm ultraviolet AlGaN multiple quantum-well laser diode. *Nat. Photon.* **2**, 551–554 (2008).
45. M. W. Knight, N. S. King, L. Liu, H. O. Everitt, P. Nordlander, N. J. Halas, Aluminum for plasmonics. *ACS Nano* **8**, 834–840 (2014).
46. H. Ehrenreich, H. R. Phillip, B. Segall, Optical properties of aluminum. *Phys. Rev.* **132**, 1918–1928 (1963).
47. W. L. Barnes, A. Dereux, T. W. Ebbesen, Surface plasmon subwavelength optics. *Nature* **424**, 824–830 (2003).
48. K. L. Tsakmakidis, T. W. Pickering, J. M. Hamm, A. F. Page, O. Hess, Completely stopped and dispersionless light in plasmonic waveguides. *Phys. Rev. Lett.* **112**, 167401 (2014).
49. K. L. Tsakmakidis, J. Hamm, T. W. Pickering, O. Hess, Plasmonic nanolasers without cavity, threshold and diffraction limit using stopped light, in *Frontiers in Optics 2012* (OSA Publishing, 2012), paper FTh2A.2.
50. H. Haken, *Synergetics* (Springer, 1983).
51. V. DeGiorgio, M. O. Scully, Analogy between the laser threshold region and a second-order phase transition. *Phys. Rev. A* **2**, 1170–1177 (1970).
52. K. L. Tsakmakidis, A. D. Boardman, O. Hess, 'Trapped rainbow' storage of light in metamaterials. *Nature* **450**, 397–401 (2007).
53. P. W. Milonni, *Fast Light, Slow Light, and Left-Handed Light* (Institute of Physics, 2005).
54. Z. Jacob, V. M. Shalaev, Plasmonics goes quantum. *Science* **334**, 463–464 (2011).
55. M. O. Scully, M. S. Zubairy, *Quantum Optics* (Cambridge Univ. Press, 2008).
56. P. K. Jha, Using quantum coherence to enhance gain in atomic physics. *Coherent Opt. Phenom.* **1**, 25 (2013).
57. B. Deveaud, A. Quattropani, P. Schwendimann, *Quantum Coherence in Solid State Systems* (IoP Press, 2009).
58. K. E. Dorfman, P. K. Jha, D.V. Voronine, P. Genevet, F. Capasso, M. O. Scully, Quantum-coherence-enhanced surface plasmon amplification by stimulated emission of radiation. *Phys. Rev. Lett.* **111**, 043601 (2013).
59. J. Hesse, T. Gross, Self-organized criticality as a fundamental property of neural systems. *Front. Syst. Neurosci.* **8**, 166 (2014).
60. H. A. Haus, *Waves and Fields in Optoelectronics* (Prentice Hall, 1984).
61. O. Hess, K. L. Tsakmakidis, Metamaterials with quantum gain. *Science* **339**, 654–655 (2013).
62. A. Pusch, S. Wuestner, J. M. Hamm, K. L. Tsakmakidis, O. Hess, Coherent amplification and noise in gain-enhanced nanoplasmonic metamaterials: A Maxwell-Bloch Langevin approach. *ACS Nano* **6**, 2420–2431 (2012).
63. R. Eisberg, R. Resnick, *Quantum Physics of Atoms, Molecules, Solids, Nuclei, and Particles* (John Wiley & Sons, 1974), pp. 232–244.
64. S. John, Localization of light. *Phys. Today* **44**, 32–40 (1991).
65. B. A. Malomed, Spatial solitons supported by localized gain. *J. Opt. Soc. Am. B* **31**, 2460–2475 (2014).
66. A. E. Siegman, Propagating modes in gain-guided optical fibers. *J. Opt. Soc. Am. A* **20**, 1617–1628 (2003).
67. V. V. Kocharovsky, V. V. Kocharovsky, M. Holthaus, C. H. R. Ooi, A. Svidzinsky, W. Ketterle, M. O. Scully, Fluctuations in ideal and interacting Bose–Einstein condensates: From the laser phase transition analogy to squeezed states and Bogoliubov quasiparticles, in *Advances in Atomic, Molecular and Optical Physics*, G. Rempe, M. O. Scully, Eds. (Academic Press, 2006), vol. 53.

Citation: K. L. Tsakmakidis, P. K. Jha, Y. Wang, X. Zhang, Quantum coherence–driven self-organized criticality and nonequilibrium light localization. *Sci. Adv.* **4**, eaaq0465 (2018).